Receive beam steering and clutter reduction for imaging the speed-of-sound inside the carotid artery

Maju Kuriakose [1], Jan-Willem Muller [2], Patrick Stähli [1], Martin Frenz [1,*] and Michael Jaeger [1]

[1] Institute of Applied Physics, University of Bern, Sidlerstrasse 5, 3012 Bern, Switzerland;

[2] Department of Biomedical Engineering, Eindhoven University of Technology, PO box 513, 5600 MB Eindhoven, The Netherlands;

* Correspondence: martin.frenz@iap.unibe.ch; Tel.: +41-31-631-8943

Abstract: Handheld imaging of the tissue's speed-of-sound (SoS) is a promising multimodal addition to diagnostic ultrasonography for the examination of tissue composition. Computed ultrasound tomography in echo mode (CUTE) probes the spatial distribution of SoS, conventionally via scanning the tissue under a varying angle of ultrasound transmission, and quantifying – in a spatially resolved way – phase variations of the beamformed echoes. So far, this technique is not applicable to imaging the lumen of vessels, where blood flow and tissue clutter inhibit phase tracking of the blood echoes. With the goal to enable the assessment of atherosclerotic plaque composition inside the carotid artery, we propose two modifications to CUTE: (a) receive (Rx) beam-steering as opposed to transmit (Tx) beam-steering to increase acquisition speed and to reduce flow-related phase decorrelation, and (b) pairwise subtraction of data obtained from repetitions of the scan sequence, to highlight blood echoes relative to static echo clutter and thus enable phase tracking of blood echoes. These modifications were tested in a phantom study, where the echogenicity of the vessel lumen was chosen similar to the one of the background medium, which allows a direct comparison of SoS images obtained with the different techniques. Our results demonstrate that the combination of Rx-steering with the subtraction technique results in a SoS image of the same quality as obtained with conventional Tx-steering. Together with the improved acquisition speed this makes the proposed technique a key step towards successful imaging of the SoS inside the carotid artery.

1. Introduction

Reliable imaging techniques for non-invasive tissue characterization are important in clinical practice for the accurate assessment of pathological and physiological abnormalities. For this purpose, multimodal imaging is often preferred over single mode imaging because it provides complementary information on a variety of different tissue parameters. On the downside, multimodal imaging can be expensive, time consuming, tedious for patients, and can suffer from image registration problems that limit the diagnostic accuracy. A promising way to overcome such drawbacks is by using a single imaging device, and extract complementary multimodal information via different ways of data acquisition/processing. Echo ultrasound (US) is already used as quick, simple and cost-effective imaging technique in many areas. To improve the diagnostic accuracy in a multimodal approach, it has recently been combined with US elastography, which allows analyzing the tissue's elastic properties [1-4]. Optoacoustic imaging, which shows blood oxygen saturation [5] [6] [7], lipid pools [8] [9] or exogenous molecular probes [10] has been implemented as an addition to conventional US [11] [12] [13] with promise for e.g. cancer diagnosis [14] [15].

45 In a similar multimodal approach, our goal is to complement the classical B-mode display of
46 echo intensity with an image of the spatial distribution of the tissue's speed of sound (SoS), both
47 derived from pulse-echo data. The SoS fundamentally depends on the tissue's compressibility and
48 density and thus a spatially resolved quantification of this parameter will help identifying
49 abnormalities in tissue compositions [16,17].
50 The diagnostic potential of imaging SoS has been thoroughly demonstrated in through-
51 transmission ultrasound tomography [18-25]. In addition, various reflection-mode techniques have
52 been investigated [26-28]. We recently developed a reflection-mode technique, named computed
53 ultrasound tomography in echo-mode (CUTE) [29,30], which allows to determine the SoS with high
54 spatial and contrast resolution in real time. The data acquisition and reconstruction scheme of CUTE
55 involves the following steps: (1) transmit (Tx) US plane waves over a range of angles (by beam
56 steering) to a region of interest, and receive (Rx) the echoes from acoustic scatterers. (2) Assuming an
57 average SoS, reconstruct (beamform) the echoes back to the hypothetical locations of the ultrasound
58 scatterers, using e.g., delay-and-sum (DAS) beamforming. (3) Detect the local echo phase shift from
59 the beamformed echoes in-between successive Tx angles and (4) finally, reconstruct the SoS image
60 from the phase shift maps. This technique is based on the following rationale: if the actual SoS inside
61 the tissue agrees with the assumed value, the round-trip times in the DAS beamforming are correctly
62 anticipated. Then, the phase of the reconstructed echoes does not depend on the Tx angle, and the
63 phase shift is zero independent of location and angle pair. If, however, the spatial distribution of SoS
64 deviates from the assumed value, it produces a corresponding phase shift due to the non-anticipated
65 round-trip time delay of the Tx transients. Using the relation between SoS and phase shift, the spatial
66 distribution of SoS can then be reconstructed by solving the corresponding inverse problem either in
67 Fourier [29] or spatial domain [31].
68 A classic use of US sonography is for diagnosing atherosclerosis [32,33] in the carotid arteries.
69 Plaques in their advanced stage may contain cellular or acellular fibrous tissues, lymphocytic
70 inflammatory infiltrate, foam cells, pultaceous debris (lipid-rich core), and calcific deposits. US
71 sonography is used for assessing plaque neovascularization, thickening of inner lining of vessel walls
72 and plaque formation. Future cardiovascular events or mortality risks can be predicted by
73 quantifying the total number of plaques [34] and plaque area or volume [35]. In addition, echogenicity
74 is used to categorize plaques into echo-lucent, predominantly echo-lucent, predominantly echogenic
75 and echogenic: Pathomorphologic studies in relation to US echogenicity suggest that low risk
76 "stable" plaques mainly consist of fibrous or calcified tissues, which appear as echogenic, while high
77 risk plaques appear as heterogeneous or translucent [36,37]. Nevertheless, the accuracy of the B-mode
78 US is still not satisfactory, and thus it is nowadays combined with US elastography to improve the
79 diagnostic accuracy.
80 Continuing this multimodal approach, CUTE is promising to aid the assessment of
81 atherosclerotic plaque rupture risk: Lipids, fibrous and calcified tissue have different SoS, thus
82 quantifying SoS will provide complementary information on plaque composition. The conventional
83 way how CUTE is performed, however, inhibits its application to the carotid artery for two reasons:
84 1. Blood motion: In conventional CUTE, Tx plane waves are sent forth to scan the full angular
85   aperture that is possible within the limits of the transducer design, e.g., from -25° to 25°. For
86   maintaining low clutter levels, synthetic Tx focusing is used, based on coherent plane wave
87   compounding [38] of acquisitions with finely spaced (e.g. 0.5°) Tx angles. Therefore,
88   conventional CUTE typically requires more than 100 acquisitions. During the time required for
89   this number of acquisitions, arterial blood flow leads to decorrelation of blood echoes, resulting
90   in phase noise and SoS artefacts.
91 2. Tissue clutter: Higher order echoes from the tissue surrounding the carotid are interpreted as
92   originating from inside the carotid, cluttering the blood echoes. Clutter has a higher intensity
93   level than the blood echoes, leading to wrong echo phase shifts and thus falsified SoS
94   reconstruction.
95 Here, we propose two modifications to the CUTE methodology that solve these problems and will
96 be an important step towards enabling imaging the SoS inside the carotid artery:

1. Rx instead of Tx beam steering for echo phase tracking, in order to reduce acquisition time and thus avoid/reduce blood flow-related artefacts. This approach is inspired by the commonly accepted principle of the reciprocity of sender and receiver, suggesting the equivalence of Tx- and Rx-steering.
2. Take benefit of blood motion to reduce clutter: Pairwise subtraction of consecutive repetitions of the signal acquisition, spaced by small (on the order of a ms) time intervals, cancels static tissue clutter and thereby highlights the decorrelating weak blood echoes.

The present phantom study demonstrates that the proposed modifications do not substantially alter the phase shift maps nor the final SoS image, compared to the conventional Tx-steering approach, making them a promising step towards SoS imaging inside the carotid artery.

2. Materials and Methods

This chapter starts with a description of conventional CUTE and of the proposed novel modifications. Although this description uses the exact acquisition parameters used in this study, it is, however, intended to be interpreted in a more general way, and different parameters may be found suitable for other specific applications (depending on hardware/sample properties). The acquisition parameters employed in this study are summarized in Table 1.

Table 1. Experimental parameters used for Tx and Rx steering

	Tx steering	full Rx	fast Rx
Tx angles	Φ = -25°:2.5°:25°	Φ = 0°	Φ = 0°
Tx aperture	Φrad = 2.5°, 0.5°steps	Φrad = 5°, 0.5°steps	Φrad = 5°, 2.5°steps
Rx angles	Ψ = 0°	Ψ = -25°:2.5°:25°	Ψ = -25°:2.5°:25°
Rx aperture	Ψrad = 5°	Ψrad = 2.5°	Ψrad = 2.5°
CUTE angles	Φcute = -25°:10°:25°	Ψ cute = -25°:10°:25°	Ψ cute = -25°:10°:25°

2.1. Conventional Tx CUTE

For conventional Tx-steering CUTE, US images were acquired for Tx steering angles ranging from -25° to 25° with a 2.5° angle step (Φ = -25°:2.5°:25°). The choice of the angle range corresponds to the desired tracking angle range. The angle limits are defined by the directional response of the transducer elements and by the element pitch. The angle step is chosen small enough to avoid phase aliasing caused by SoS variations.

For Rx beamforming, an angular aperture with radius Ψrad = 5° was used, centred on the Rx angle Ψ = 0°. To generate images with a clutter level enabling robust phase tracking, focusing is required in Tx. One way to achieve Tx focusing is to scan the sample with an actually focused beam (line-by-line scan), which however results in an unnecessarily large number of acquisitions especially as multiple focal depths are required. A far more efficient way to achieve Tx focusing is coherent plane-wave compounding. This was done for each tracking angle, from a group of plane-wave acquisitions centred on the respective tracking angle with a Tx aperture radius Φ rad = 2.5° and a 0.5° step size. This resulted in a total plane wave Tx angle range of [-27.5°:0.5°:27.5°], i.e. 111 acquisitions. The coherently compounded images, 11 in total, were then used for phase tracking.

2.2. Full-Rx CUTE

Rx tracking can be implemented in a very similar way to the conventional Tx tracking, by interchanging the Tx and Rx parameters. The Rx angular aperture of the conventional approach was thus replaced by an identical Tx angular aperture in the Rx approach. For this purpose, plane wave acquisitions were performed with Tx angles ranging within an aperture radius Φ rad = 5° centred around Φ = 0° at 0.5° step size, resulting in 21 acquisitions. This already provides a factor 5 reduction

138 in acquisition time, reducing blood-flow and tissue-motion related phase tracking errors. For each Tx
139 angle, a set of 21 Rx-steered images was reconstructed, using steering angles (Ψ = -25°:2.5°:25°) with
140 an Rx angular aperture radius Ψ rad = 2.5°, resulting in 21 times 21 Tx- and Rx-steered plane wave
141 images. Then, synthetic Tx focusing was achieved for each Rx-steering angle separately, by
142 coherently compounding over the 21 different Tx angles, resulting in the desired 21 Rx-steered (and
143 Tx-focused) images for phase tracking.
144 This approach, where the Rx aperture of conventional CUTE is replaced with a quasi-continuous
145 Tx aperture in the Rx-steering approach, is hereafter termed as 'full-Rx CUTE'.

146 *2.3. Fast-Rx subtraction technique*

147 Preliminary in-vivo results of carotid imaging indicate that the total time needed for all
148 acquisitions in full-Rx CUTE is still too long, resulting in substantial flow-related echo decorrelation
149 during scanning the Tx angle range and thus to phase noise in the coherently compounded images.
150 Such flow-related decorrelation can be reduced by a further reduction of the number of Tx angles.
151 Reducing the number of Tx angles on the other hand increases phase noise, caused by clutter
152 stemming from tissue surrounding the artery, which obscures the comparably weak blood echoes.
153 To solve this problem, we propose to make use of the blood flow: multiple data sets (each
154 containing the same Tx angle range) are acquired, with a long enough time delay in-between
155 consecutive repetitions allowing the blood echoes to decorrelate while echoes from surrounding
156 tissue remain static. By subtracting successive data sets, stationary tissue clutter is reduced (ideally
157 to zero), whereas the decorrelating blood echoes remain visible. The important point here is that
158 blood echo decorrelation occurs in-between data sets, but not substantially within each data set.
159 Preliminary in-vivo results indicated that a number of 5 acquisitions per data set is sufficiently small
160 to reduce blood echo decorrelation to an acceptable level. For our phantom study, we therefore used
161 a Tx angle step of 2.5°, resulting in a total of 5 angles distributed over the desired Tx angle range from
162 -5° to 5°.
163 The subtraction technique can only provide echoes from inside the vessel, not from the
164 surrounding static tissue. To allow phase shift tracking over the whole image area, the segmented
165 echoes from inside the blood vessel, obtained with the fast-Rx subtraction approach, were therefore
166 combined with the echoes from the surrounding tissue, obtained with the full-Rx approach.
167
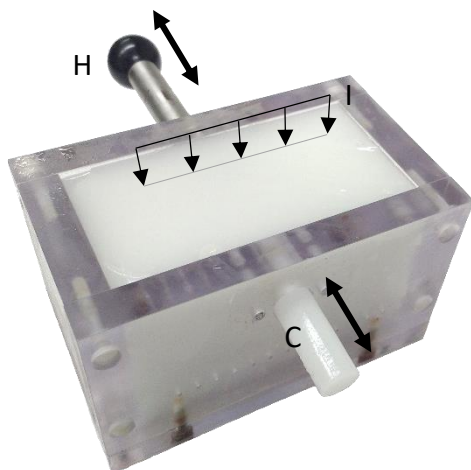
169 **Figure 1.** Photograph of the phantom, indicating the location of the imaging plane I. The artery-
170 mimicking cylindrical inclusion C could be manually moved by moving the handle H.

171 *2.4. Phantom description*

172 The experiments were conducted using an agar-cellulose phantom, where agar formed the gel
173 network and cellulose provided echogenicity for US. This phantom consisted of a background with
174 uniform SoS, into which a movable cylindrical inclusion was inserted having a positive SoS contrast

175 compared to the background. The inclusion had a diameter of 7 mm and was placed at 10 mm depth
176 below the phantom surface (Fig.1) to imitate a carotid artery. Blood flow was simulated by manually
177 moving the inclusion.
178
179 The phantom was prepared by slowly adding 2 wt% of agar powder (Sigma–Aldrich, Germany)
180 and 2 wt% of cellulose powder (20-micrometer, Sigma–Aldrich, Germany) into continually stirred
181 deionized water at room temperature to avoid lumps. The solution was heated above 80° C (melting
182 temperature of agar) and degassed by exposing it to a vacuum level of about 0.1 atm for about 5
183 minutes. After cooling down to about 40 °C, ethanol (1 vol%) was added for adjusting the SoS of the
184 background to the desired value of 1490 m/s. This final solution was poured (while still at 40 °C) into
185 a pre-cooled mould, which contained a removable steel rod with 7 mm diameter at the location where
186 the cylindrical inclusion was to be inserted later on. The mould was then quickly cooled down below
187 the gelation temperature (30°) to minimise sedimentation of cellulose during gelation. All
188 experiments were performed at ambient temperature (22 °C). In a different mould, a cylindrical
189 inclusion with 7 mm diameter was prepared with 2% cellulose following the same procedure and by
190 adding 5 vol.% of ethanol to generate a positive SoS contrast (SoS=1540 m/s). The cylindrical inclusion
191 was inserted into the background sample only for the time of the experiment to avoid diffusion of
192 ethanol between the inclusion and the background, which would else level off the SoS contrast.

193 *2.4. Acquisition system*

194 The experiments were performed using a Vantage 64 LE ultrasound system (Verasonics,
195 Redmond, WA, USA). The ultrasound probe was a Philips L12-5 linear array probe (ATL Bothell,WA,
196 USA) having a 0.19 mm element pitch. Matlab (The MathWorks, MA, USA) software was used to
197 program the acquisition and the off-line image reconstruction. The probe was placed on the top
198 surface of the phantom with the imaging plane aligned perpendicular to the cylindrical inclusion
199 (Fig. 1). The transducer was driven at 9 MHz transmit centre frequency. Raw radio-frequency (rf)
200 data were collected with a fourfold sampling frequency of 36 MHz.

201 *2.5. US image reconstruction and phase tracking*

202 The signal processing starts with the conversion of the rf data into reconstructed complex rf (crf)
203 mode images applying the Hilbert transformation followed by DAS beamforming.
204 An important prerequisite for proving the experimental equivalence between Tx- and Rx-
205 steering is the mathematical equivalence of the implementation of the DAS algorithms. In both the
206 Tx- and the Rx-CUTE approaches, Tx beamforming was achieved via coherent compounding of plane
207 wave transmission data. Conventionally, Rx-beamforming is implemented via summation over
208 subsets of transducer elements. This approach is, however, not mathematically equivalent to plane
209 wave compounding, as the elements have spherical/cylindrical receiving fields as opposed to the
210 plane transmitted fields. To achieve mathematical equivalence, we therefore implemented an
211 adapted way of DAS beamforming, consisting of two stages: In a first stage, the element-wise rf data
212 was converted to receive angle-wise rf data, using a DAS algorithm with linear delay profiles (as
213 opposed to focused delay profiles) and summation over the full array aperture as done in a classical
214 phased-array sector scan. This was done for delay profiles corresponding to Rx angles ranging from
215 -27.5° to 27.5° in 0.5° steps, resulting in receiving fields that were identical with the transmitting fields
216 used for synthetic Tx beamforming. In a second stage, the angle-wise rf data was coherently
217 compounded over the desired Rx angular apertures.
218 Echo phase shift maps were obtained using Loupas-type phase correlation [39]: The crf image at
219 the n-th tracking angle was point-wise multiplied with the complex conjugate of the crf mode image
220 at the adjacent (n+1)-th angle. The complex product was convolved with a spatial low-pass filter
221 kernel having dimensions of 1 mm by 1 mm. The phase angle of the filtered complex product was
222 regarded as proportional to the spatially-resolved, non-anticipated time-of-flight (ToF) differences
223 along the different tracking angles (phase shift map). Any deviation of the medium's SoS from the
224 assumed value c_0 would result in non-zero phase shift values.

225 *2.6. SoS image reconstruction*

226   For SoS reconstruction, groups of two adjacent phase shift maps were summed up, to obtain
227 phase shift maps for a reduced number of final tracking angles, i.e. [-25°:10°:25°]. The step size of 10°
228 was a compromise between artefact level and numerical efficiency of SoS reconstruction: In our
229 experience, SoS artefacts typically decrease with increasing number of angles, but converge below a
230 10° angle step. A linear space domain algorithm was used for SoS image reconstruction, assuming
231 straight ray US propagation: In the forward model, the echo phase shift values were expressed as a
232 function of line integrals of slowness deviation (i.e. the difference between actual slowness and
233 assumed slowness, where the slowness is defined as inverse of SoS) in a system matrix. A Tikhonov
234 pseudo-inverse of the system matrix was calculated, with L2 norm regularization of the slowness
235 gradient, to reconstruct the slowness deviation from the measured phase shift data.

236 **3. Results**

237 *3.1. Tx versus full-Rx CUTE*

238   The first goal of this study was to demonstrate the experimental equivalence between the Tx- and the
239 full Rx-steering approach. Fig. 2a and 2b show the echo phase shift maps obtained with the two
240 approaches. The images show visually very similar results. A comparison of the rms value of the
241 difference between the phase shifts of the two approaches, with the rms value of the phase shifts of
242 the Tx-steering approach, yields a ratio of 0.05, quantitatively supporting the close similarity of both
243 results. Fig. 2c and 2d show the SoS images resulting from the Tx- and the full Rx-steering approach,
244 respectively. Note that the color maps account for an offset of -8 m/s of the full-Rx compared to the
245 Tx result. Apart from this offset, the reconstructed spatial distribution of the SoS looks very similar:
246 Both images reveal the positive SoS contrast at the location of the cylindrical inclusion. Below the
247 inclusion, both techniques show comparable artefacts. These artefacts originate from phase noise due
248 to aberrations (refraction) of US propagating through the inclusion. The disagreement at the upper
249 edge of the image near the transducer aperture can be attributed to phase noise due to element cross-
250 talk, when transmitting on different transducer elements with different time delays. This phase noise
251 plays a different role in the two approaches because of the different Tx angle ranges.
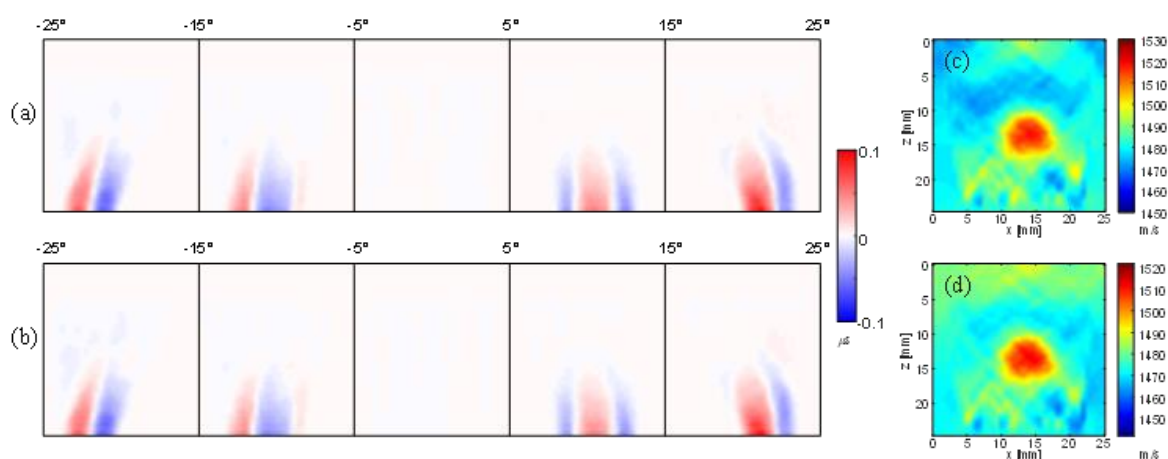
252

253 **Figure 2.** Comparison of Conventional Tx and full-Rx steering. (**a**) Phase shift maps from Tx steering;
254   (**b**) Phase shift maps from full-Rx steering; (**c**) SoS image from Tx steering; (**e**) SoS image from full-Rx
255   steering. Note the 8 m/s difference between the color scales in (c) and (d).

256 *3.2. Fast-Rx subtraction technique*

257 Preliminary volunteer results of full-Rx echo phase tracking using 21 Tx angles indicated that even
258 the reduced acquisition time is still long enough that blood echo decorrelation still occurs. To further
259 reduce the acquisition time, the fast-Rx approach reduces the quasi-continuous Tx aperture to only 5

260 Tx angles. While reducing echo decorrelation, this however results in reduced synthetic Tx focus
261 quality, and thus increased clutter level. This effect is visible in the phantom study, where the angle
262 number reduction led to increased phase noise in the echo phase shift maps (Fig. 3a), compared to
263 the full-Rx approach (Fig. 2b). As a result, the SoS image shows a high level of artefacts and an
264 inaccurate spatial distribution of SoS inside the inclusion (Fig. 3b).

265 Most of the clutter found inside the inclusion area consists of stationary higher-order echoes
266 originating from outside the inclusion. The subtraction technique aims at reducing this stationary
267 clutter via pairwise subtracting consecutively repeated fast-Rx acquisitions. At the same time, blood
268 flow between the sequence repetitions avoids cancellation of blood echoes, thus highlighting the
269 blood echo intensity compared to stationary echoes. This is illustrated by B-mode US images:
270 Whereas the echogenicity inside the inclusion was slightly lower than in the background in the non-
271 subtracted data (Fig. 3c), the subtraction data highlights the echoes from inside the inclusion (Fig.
272 3d). The reduced intensity level of the stationary echoes outside the inclusion results in a reduced
273 relative level of clutter inside the inclusion. The difference data thus allows robust phase tracking
274 inside the inclusion in spite of the reduced number of angles. Outside the inclusion, however, the
275 relative clutter level stays unchanged.

276 To enable echo phase tracking both in- and outside the inclusion, the fast-Rx subtraction data from
277 inside the inclusion is combined with full-Rx data from outside the inclusion. The second goal of this
278 study was to demonstrate that this combination allows reconstructing the SoS in a similar way as
279 when high-quality (full-Rx) echoes would be available also inside the inclusion. The segmentation
280 was achieved by manual selection of centre point and radius of the inclusion area. The fast-Rx
281 subtraction data was scaled with a factor 10 before combination to account for intensity differences.
282 For illustration, Fig. 3e shows a B-mode US image resulting from this combination, where an equal
283 echogenicity both in- and outside the lumen area was achieved. Fig. 3f shows the SoS image that was
284 reconstructed from the resulting echo phase shift maps. Only minor differences are seen between the
285 spatial distribution of reconstructed SoS in this image, compared to the one obtained with full-Rx
286 CUTE alone (Fig. 2d).
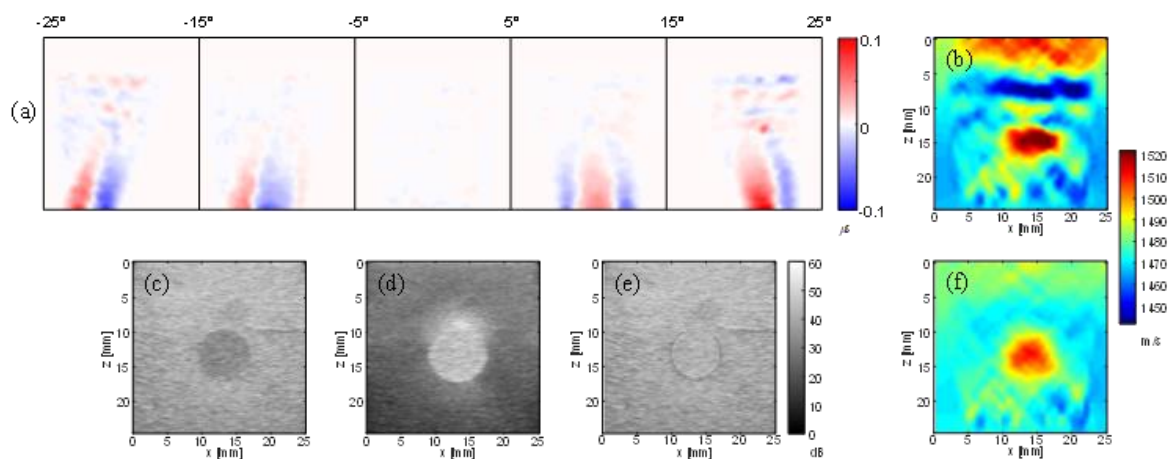
Figure 3. (**a**) Phase shift maps from fast-Rx approach alone; (**b**) SoS image obtained from the fast-Rx approach without subtraction; (**c**) B-mode US image from full-Rx data; (**d**) B-mode US image from subtracted fast-Rx data; (**e**) Combined B-mode US image; (**f**) SoS image from combined data. Note that in (c) to (e), the dB scale is normalized to the maximum intensity level in each image.

4. Discussion and conclusion

293 The first part of this study shows that the conventional Tx-steering approach can be substituted by
294 the less time-consuming full-Rx approach (see Fig. 2). Due to the ill-posed inverse problem of
295 reconstructing the SoS from echo phase shift, small differences in echo phase shift can in principle be

reflected in more notable differences in the SoS images. In spite of that, the spatial distribution of SoS in and around the lumen-mimicking inclusion was similar between the two approaches. The small SoS offset of -8 m/s of the full-Rx compared to the Tx approach can be attributed to remaining experimental differences, e.g. due to the different way how the transducer's piezoelectric elements couple to the acoustic lens on reception than on transmission.

To avoid echo decorrelation due to blood flow, an in-vivo scenario requires a short acquisition time and thus a low number of Tx angles. A low number of Tx angles, however, increases tissue clutter which obscures blood echoes. The second part of the study (see Fig. 3) demonstrates that a reduction of acquisition time is possible with simultaneously reduced clutter if using the fast-Rx subtraction approach: Echo phase tracking inside the lumen becomes possible using only 5 Tx angles. The combination of this data with full-Rx data from outside the lumen results in a correct SoS image, in the sense that it agrees with the one obtained with full-Rx CUTE alone.

A clinical situation, however, differs from the presented phantom study in several aspects, which require attention when aiming at an in-vivo implementation of the proposed technique:

1. In the phantom, the simulated flow speed was identical across the lumen cross-section. In an in-vivo scenario, blood in the center of the lumen moves faster than blood near the periphery. So, a simple subtraction would lead to non-uniform echo strength, converging to zero towards the vessel wall. The subtraction corresponds to a linear ramp filter in the frequency domain of the "slow" time axis (repetitions of acquisitions). To achieve a more uniform echo level, one may make use of wall filters, similar to what is used in Doppler flow imaging.

2. In an in-vivo scenario, the background tissue is not perfectly stationary due to pulsating blood flow, which will lead to residual "stationary" clutter inside the vessel lumen even after subtraction. One strategy to minimize motion is by choosing an optimum timing of the fast-Rx acquisitions in-between successive heart beats. This can be achieved by synchronizing the acquisition with a motion detection algorithm or an ECG. A different and complementary strategy is motion tracking and motion compensation before subtraction or wall filtering.

3. The low SNR of blood echoes can produce phase noise and thus artefacts in the SoS reconstruction. SNR can be improved by repeating the fast-Rx acquisition multiple times similar to what is done in Doppler flow imaging, and averaging the phase correlation maps before determining the echo phase shift.

4. In our present study, lumen motion occurred only in-between repetitions, but not during a single acquisition sequence. In an in-vivo situation, blood flow occurs during the few plane wave transmissions of each single fast-Rx acquisition sequence. Even though the number of Tx angles is short enough so that echo decorrelation does not occur, the blood motion will add a phase shift bias. One strategy to reduce this influence is to invert the Tx angle sequence in successive fast-Rx acquisitions, so that the phase shift due to blood flow cancels out in the final average phase shift.

In summary, the developed technique is a key step towards imaging the SoS inside arteries, in spite of blood flow and tissue clutter that obscures the hypoechoic blood echoes. This becomes possible via shortening the length of the acquisition sequence and via reducing stationary clutter using the subtraction approach. Whereas the envisaged goal of this study was to enable imaging the SoS inside the carotid artery, the developed technique may have further importance, e.g. for the assessment of iliac artery stenosis, or in liver imaging for reducing SoS artefacts that occur around the hepatic veins, vena cava, portal vein and the hepatic artery.

Author Contributions: Conceptualization, M.J; methodology, M.K., and J.-W.M.; software, M.K. and M.J.; validation, M.K.; formal analysis, M.J.; investigation, M.K. and J.-W.M.; resources, M.F.; data curation, M.J.;

References

353

354 1.   Kato, K.; Sugimoto, H.; Kanazumi, N.; Nomoto, S.; Takeda, S.; Nakao, A. Intra-operative application of
355   real-time tissue elastography for the diagnosis of liver tumours. *Liver International* **2008**, *28*, 1264-1271.

356 2.   Bercoff, J.; Tanter, M.; Fink, M. Supersonic shear imaging: A new technique for soft tissue elasticity
357   mapping. *IEEE Trans Ult Ferr Freq Cont* **2004**, *51*, 396-409.

358 3.   Hall, T.J.; Zhu, Y.; Spalding, C.S. In vivo real-time freehand palpation imaging. *Ult Med Biol* **2003**, *29*,
359   427-435.

360 4.   Shiina, T.; Nitta, N.; Ueno, E.; SJSUM; Bamber, J.C. Real time tissue elasticity imaging using the
361   combined autocorrelation method. *J Med Ult* **2002**, *26*, 57-66.

362 5.   Laufer, J.; Delpy, C.; Elwell, P.; Beard, P. Quantitative spatially resolved measurement of tissue
363   chromophore concentrations using photoacoustic spectroscopy: application to the measurement of
364   blood oxygenation and haemoglobin concentration. *Phys Med Biol* **2007**, *52*, 141-168.

365 6.   Held, K.G.; Jaeger, M.; Ricka, J.; Frenz, M.; Akarcay, H.G. Multiple irradiation sensing of the optical
366   effective attenuation coefficient for spectral correction in handheld OA imaging. *Photoacoustics* **2016**, *4*,
367   70-80.

368 7.   Cox, B.; Laufer, J.G.; Arridge, S.R.; Beard, P.C. Quantitative spectroscopic photoacoustic imaging: a
369   review. *J Biomed Opt* **2012**, *17*, 0612021-06120222.

370 8.   Jansen, K.; van Soest, G.; van der Steen, A.F.W. Intravascular photoacoustic imaging: a new tool for
371   vulnerable plaque identification. *Ult Med Biol* **2014**, *40*, 1037-1048.

372 9.   Wu, M.; Jansen, K.; van der Steen, A.F.W.; van Soest, G. Specific imaging of atherosclerotic plaque lipids
373   with two-wavelength intravascular photoacoustics. *Biomed Opt Exp* **2015**, *6*, 3276-3286.

374 10.   Weber, J.; Beard, P.C.; Bohndiek, S.E. Contrast agents for molecular photoacoustic imaging. *Nature*
375   *Methods* **2016**, *13*, 639-650.

376 11.   Niederhauser, J.J.; Jaeger, M.; Lemor, R.; Weber, P.; Frenz, M. Combined ultrasound and optoacoustic
377   system for real-time high-contrast vascular imaging in vivo. *IEEE Trans Med Imaging* **2005**, *24*, 436-440.

378 12.   Daoudi, K.; van den Berg, P.J.; Rabot, O.; Kohl, A.; Tisserand, S.; Brands, P.; Steenbergen, W. Handheld
379   probe integrating laser diode and ultrasound transducer array for ultrasound/photoacoustic dual
380   modality imaging. *Opt Express* **2014**, *22*, 26365-26374.

381 13.   Singh, M.K.A.; Steenbergen, W.; Manohar, S. Handheld probe-based dual mode
382   ultrasound/photoacoustics for biomedical imaging. In *Frontiers in Biophotonics for Translational Medicine*,
383   Springer: Singapore, 2016; pp. 209-247.

14. Laufer, J.; Johnson, P.; Zhang, E.; Treeby, B.; Cox, B.; Pedley, B.; Beard, P. In vivo preclinical photoacoustic imaging of tumor vasculature development and therapy. *J Biomed Opt* **2012**, *17*, 0560161-0560168.

15. Toi, M.; Asao, Y.; Matsumoto, Y.; Sekiguchi, H.; Yoshikawa, A.; Takada, M.; Kataoka, M.; Endo, T.; Kawaguchi-Sakita, N.; Kawashima, M., et al. Visualization of tumor-related blood vessels in human breast by photoacoustic imaging system with a hemispherical detector array. *Scientific Reports* **2017**, *7*, 41970--41971-41911.

16. Sarvazyan, A.P.; Urban, M.W.; Greenleaf, J.F. Acoustic waves in medical imaging and diagnostics. *Ult Med Biol* **2013**, *39*, 1133-1146.

17. Bamber, J.C.; Hill, C.R.; King, J.A. Acoustic properties of normal and cancerous human liver-II Dependence on tissue structure. *Ult Med Biol* **1981**, *7*, 135-144.

18. Greenleaf, J.F.; Bahn, R.C. Clinical imaging with transmissive ultrasonic computerized tomography. *IEEE Trans Biomed Eng* **1981**, *28*, 177-185.

19. Carson, P.; Meyer, C.; Scherzinger, A.; Oughton, T. Breast imaging in coronal planes with simultaneous pulse-echo and transmission ultrasound. *Science* **1981**, *214*, 1141-1143.

20. Scherzinger, A.; Belgam, R.; Carson, P.; Meyer, C.; Sutherland, J.; Bookstein, F.; Silver, T. Assessment of ultrasonic computed tomography in symptomatic breast patints by discriminant analysis. *Ult Med Biol* **1989**, *15*, 21-28.

21. Duric, N.; Littrup, P.; Poulo, L.; Babkin, A.; Pevzner, R.; Holsapple, E.; Rama, O.; Glide, C. Detection of breast cancer with ultrasound tomography: First results with the computed ultrasound risk evaluation (CURE) prototype. *Med Phys* **2007**, *34*, 773-785.

22. Wiskin, J.; Borup, D.; Johnson, S.; Berggren, M. Non-linear inverse scattering: High resolution quantitative breast tissue tomography. *J Acoust Soc Am* **2012**, *131*, 3802-3813.

23. Nebeker, J.; Nelson, T.R. Imaging of sound speed using reflection ultrasound tomography. *J Ultrasound Med* **2012**, *31*, 1389-1404.

24. Ruiter, N.V.; Zapf, M.; Dapp, R.; Hopp, T.; Kaiser, W.A.; Gemmeke, H. First results of a clinical study with 3D ultrasound computer tomography. *IEEE Int Ult Symp* **2013**.

25. Zografos, G.; Liakou, P.; Koulocheri, D.; Liovarou, I.; Sofras, M.; Hadjiagapis, S.; Orme, M.; Marmarelis, V. Differentiation of BIRADS-4 small breast lesions via multimodal ultrasound tomography. *Eur Radiol* **2015**, *25*, 410-418.

26. Robinson, D.E.; Ophir, J.; Wilson, L.S.; Chen, C.F. Pulse-echo ultrasound speed measurements: Progress and prospects *Ult Med Biol* **1991**, *17*, 633-646.

27. Shin, H.-C.; Prager, R.; Gomersall, H.; Kingsbury, N.; Treece, G.; Gee, A. Estimation of average speed of sound using deconvolution of medical ultrasound data. *Ult Med Biol* **2010**, *36*, 623-636.

28. Anderson, M.E.; Trahey, G.E. The direct estimation of sound speed using pulse-echo ultrasound. *J Acoust Soc Am* **1998**, *104*, 3099-3106.

29. Jaeger, M.; Held, G.; Peeters, S.; Preisser, S.; Grünig, M.; Frenz, M. Computed ultrasound tomography in echo mode for imaging speed of sound using pulse-echo sonography: Proof of principle *Ult Med Biol* **2015**, *41*, 235-250.

30. Jaeger, M.; Robinson, E.; Akarçay, H.; Frenz, M. Full correction for spatially distributed speed-of-sound in echo ultrasound based on measuring aberration delays via transmit beam steering. *Phys Med Biol* **2015**, *60*, 4497-4515.

426   31.   Jaeger, M.; Frenz, M. Quantitative imaging of speed of sound in echo ultrasonography. In Proceedings
427   of IEEE Int Ult Symp

428   32.   Lukanova, D.; Nikolov, N.; Genova, K.; Stankev, M.; Georgieva, E. The accuracy of noninvasive
429   imaging techniques in diagnosis of carotid plaque morphology. *OA Maced J Med Sci* **2015**, *3*, 224-230.

430   33.   Park, T. Evaluation of carotid plaque using ultrasound imaging *J Cardiovasc Ultrasound* **2016**, *24*, 91-95.

431   34.   Störk, S.; Feelders, R.A.; van den Beld, A.W.; Steyerberg, E.W.; Savelkoul, H.F.J.; Lamberts, S.W.J.;
432   Grobbee, D.E.; Bots, M.L. Prediction of mortality risk in the elderly *Am J Med* **2006**, *119*, 519-525.

433   35.   Steinl, D.C.; Kaufman, B.A. Ultrasound imaging for risk assessment in atherosclerosis. *Int J Mol Sci* **2015**,
434   *16*.

435   36.   Schulte-Altedorneburg, G.; Droste, D.; Haas, N.; Kemény, V.; Nabavi, D.; Füzesi, L.; Ringelstein, E.
436   Preoperative B-mode ultrasound plaque appearance compared with carotid endarterectomy specimen
437   histology. *Acta Neurol Scand* **2000**, *101*, 188-194.

438   37.   Reiter, M.; Horvat, R.; Puchner, S.; Rinner, W.; Polterauer, P.; Lammer, J.; Minar, E.; Bucek, R.A. Plaque
439   imaging of the internal carotid artery - Correlation of B-flow imaging with histopathology. *AJNR* **2007**,
440   *28*, 122-126.

441   38.   Tanter, M.; Fink, M. Ultrafast imaging in biomedical ultrasound. *IEEE Trans Ult Ferr Freq Cont* **2014**, *61*,
442   102-119.

443   39.   Loupas, T.; Powers, J.T.; Gill, R.W. An axial velocity estimator for ultrasound blood flow imaging, based
444   on a full evaluation of the Doppler equation by means of a two-dimensional autocorrelation approach.
445   *IEEE Trans Ult Ferr Freq Cont* **1995**, *42*, 672-688.

449